ESO Science Archive Facility - Phase 3 Data Release Description
ESO programme 3D Mapping of the Dynamic Feedback and Chemistry in the Star Formation Process across Galaxy Disks, Data Release DR1
provided by E. Schinnerer, published on 2021-07-16

PHANGS-MUSE: 3D Mapping of the Dynamics, Feedback and Chemistry in the Star Formation Process across Galaxy Disks

Abstract

We present the PHANGS-MUSE observational programme, a survey using the MUSE integral field spectrograph at the VLT to map 19 star-forming disk galaxies (Emsellem et al. 2021). The released data is mainly based on ESO programmes 1100.B-0651, 095.C-0473, and 094.C-0623 (PHANGS-MUSE), and includes a few exposures from five archival programmes (094.B-0321, MAGNUM; 099.B-0242, 0100.B-0116, 098.B-0551, MAD; 097.B-0640, TIMER). Observations were taken in the wide field mode (WFM) with nominal wavelength coverage, with a mix of AO and non-AO targets, and multiple MUSE pointings which are combined to mosaic the central star-forming disks of each galaxy. Typical seeing ranges from 0.7-1 arcsecond. With this document, we release astrometrically aligned and (absolute) flux calibrated mosaiced data cubes that combine multiple MUSE pointings, and encompass the entire field of view observed in each galaxy. We also release maps of derived data products, including emission line fluxes and kinematics, as well as stellar kinematics. For both the data cubes and the maps, we release a version at native resolution, as well as a version that has been homogenized such that all pointings across any individual galaxy and across wavelengths are convolved to a matched angular resolution. Together with dedicated ALMA and HST observations delivering exquisite information regarding, e.g., giant molecular clouds and star clusters, the MUSE campaign provides a comprehensive view of the chemo-dynamical evolution of the star formation process across the different environments, addressing timescales associated with star formation, quantifying the importance of stellar feedback, studying the chemical enrichment and mixing, and connecting the local conditions with the large-scale dynamics.

Overview of Observations

This data release is based primarily on data observed as part of the PHANGS-MUSE Large Program (1100.B-0651). These 18 galaxies are supplemented by a pilot target, NGC0628 (095.C-0473 and 094.C-0623) to make up the full set of 19 galaxies that comprise the sample (see Figure 1). For some galaxies, existing archival data was also incorporated into our mosaic (from 094.B-0321, MAGNUM; 099.B-0242, 0100.B-0116, 098.B-0551, MAD; 097.B-0640, TIMER). For more details see Emsellem et al. (2021). Shown below (Figure 1) are the positions of each individual pointing: each galaxy was observed in WFM with the nominal wavelength coverage. 9 of the more distant galaxies were observed with AO correction (as labelled). The white vertical bar on the left side of each panel represents 5 kpc.

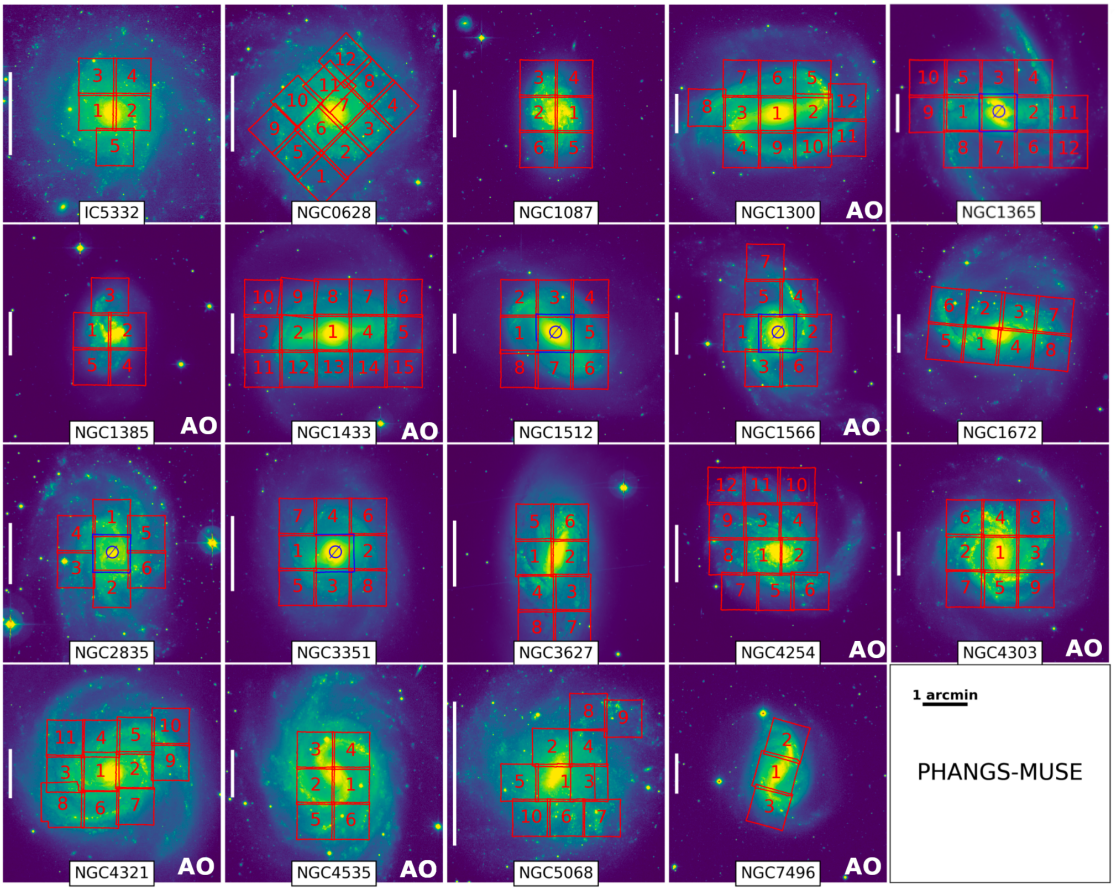

Figure 1: *Footprints for the MUSE observations of PHANGS galaxies. Each panel represents one target of the PHANGS-MUSE sample, with a 5 × 5 arcmin2 field of view from the WFI Rc -band images (r-band DuPont for NGC 7496), and the footprints of the MUSE exposures overlaid in red. Pointings marked with the ∅ symbol (in NGC 1365, NGC 1512, NGC 1566, NGC 2835, NGC 3351) and outlined in blue correspond to observations acquired outside of the main PHANGS campaign, but reduced following the same data flow and released as part of PHANGS-MUSE. The vertical white bar on the left side of each panel indicates a scale of 5 kpc.*

Release Content

The following galaxies are included in this Data Release:

Table 1: *the PHANGS-MUSE sample. Basic properties of the PHANGS-MUSE galaxies, and some characteristics of the MUSE observations.*

Name	Distance[a] [Mpc]	Log($M_\star$)[b] [$M_\odot$]	Log(SFR)[b] [$M_\odot$ yr^{-1}]	E(B-V)$_{MW}$[c] [mag]	scale [pc/arcsec]	PSF[d] [arcsec]	copt PSF[e] [arcsec]
IC5332	9.0	9.67	-0.39	0.015	43.7	$0.72\pm^{0.08}_{0.12}$	0.87
NGC0628	9.8	10.34	0.24	0.062	47.7	$0.73\pm^{0.11}_{0.13}$	0.92
NGC1087	15.9	9.93	0.12	0.030	76.8	$0.74\pm^{0.10}_{0.12}$	0.92
NGC1300	19.0	10.62	0.07	0.026	92.1	$0.63\pm^{0.18}_{0.13}$	0.89
NGC1365	19.6	10.99	1.23	0.018	94.9	$0.82\pm^{0.26}_{0.24}$	1.15
NGC1385	17.2	9.98	0.32	0.018	83.5	$0.49\pm^{0.10}_{0.11}$	0.67
NGC1433	18.6	10.87	0.05	0.008	90.3	$0.65\pm^{0.18}_{0.14}$	0.91
NGC1512	18.8	10.71	0.11	0.009	91.3	$0.80\pm^{0.38}_{0.16}$	1.25
NGC1566	17.7	10.78	0.66	0.008	85.8	$0.64\pm^{0.09}_{0.10}$	0.80
NGC1672	19.4	10.73	0.88	0.021	94.1	$0.72\pm^{0.17}_{0.08}$	0.96
NGC2835	12.2	10.00	0.09	0.089	59.2	$0.85\pm^{0.23}_{0.18}$	1.15
NGC3351	10.0	10.36	0.12	0.024	48.3	$0.74\pm^{0.24}_{0.13}$	1.05
NGC3627	11.3	10.83	0.58	0.029	54.9	$0.77\pm^{0.21}_{0.10}$	1.05
NGC4254	13.1	10.42	0.49	0.035	63.5	$0.58\pm^{0.23}_{0.14}$	0.89
NGC4303	17.0	10.52	0.73	0.020	82.4	$0.58\pm^{0.12}_{0.07}$	0.78
NGC4321	15.2	10.75	0.55	0.023	73.7	$0.64\pm^{0.45}_{0.18}$	1.16
NGC4535	15.8	10.53	0.33	0.017	76.5	$0.44\pm^{0.03}_{0.01}$	0.56
NGC5068	5.2	9.40	-0.56	0.091	25.2	$0.73\pm^{0.23}_{0.21}$	1.04
NGC7496	18.7	10.00	0.35	0.008	90.8	$0.79\pm^{0.03}_{0.17}$	0.89

Notes. [a] From the compilation of Anand et al. (2021). [b] Derived by Leroy et al. (2021), using *GALEX* UV and *WISE* IR photometry, following a similar methodology to Leroy et al. (2019). [c] Based on Schlafly & Finkbeiner (2011) [d] FWHM of the Moffat PSF across individual pointing (we report the mean and the minimum and maximum values in the R band). [e] FWHM of the Gaussian PSF of the homogenized ('copt') mosaic.

A full list of pointings is given below (see Table 2). In the following table we report the galaxy and pointing ID (column 1), sky coordinates of the pointing (columns 2 and 3), day and starting time of the OB (column 4), progressive number (increasing with the exposure observing time) of the science exposures part of the OB and included in the final mosaic (column 5), PSF FWHM estimated using the final OB data cube (column 6), and MUSE observation mode (column 7).

Table 2: *Detailed account of all pointings taken in the course of the PHANGS-MUSE survey.*

Galaxy & Pointing ID	RA [°/]	DEC [°]	TPL start	Exposure #	PSF (FWHM) [″]	MUSE mode WFM
IC5332 P01	353.622663	-36.10046	2018-06-14T08:00:41	1-2-3-4	0.59	noAO
IC5332 P02	353.603097	-36.10029	2018-07-11T06:07:18	1-2-3-4	0.80	noAO
IC5332 P03	353.622731	-36.08404	2018-07-11T08:14:50	1-2-3-4	0.67	noAO
IC5332 P04	353.60243	-36.0847	2018-07-11T09:18:27	1-2-3-4	0.72	noAO
IC5332 P05	353.612201	-36.117	2018-07-12T07:19:22	1-2-3-4	0.75	noAO
NGC0628 P01	24.179717	15.75473	2015-09-15T05:00:21	1-2-3	0.73	noAO
NGC0628 P02	24.168492	15.76554	2017-07-22T07:36:21	1-2-3	0.77	noAO
NGC0628 P03	24.157267	15.77634	2017-07-25T07:31:28	1-2	0.73	noAO
			2017-11-13T03:43:40	1-2-3		
NGC0628 P04	24.146037	15.78714	2017-09-16T04:17:06	1-2-3	0.84	noAO
NGC0628 P05	24.190942	15.76554	2016-12-30T01:01:19	1-2-3	0.74	noAO
NGC0628 P06	24.179717	15.77634	2016-10-01T04:56:00	1	0.62	noAO
			2016-10-01T05:21:15	1-2		
NGC0628 P07	24.168492	15.78714	2016-10-01T06:08:00	1-2-3	0.60	noAO
NGC0628 P08	24.157262	15.79794	2017-07-21T08:25:39	1-2-3	0.69	noAO
NGC0628 P09	24.202171	15.77634	2017-11-13T01:22:29	1-2-3	0.70	noAO
NGC0628 P10	24.191146	15.78908	2014-10-31T03:39:46	1-2-3	0.75	noAO
NGC0628 P11	24.175675	15.79605	2014-10-31T04:40:25	1-2-3	0.74	noAO
NGC0628 P12	24.168492	15.80875	2017-11-13T02:32:55	1-2-3	0.66	noAO
NGC1087 P01	41.596158	-0.49892	2017-11-13T04:56:31	1-2-3-4	0.69	noAO
NGC1087 P02	41.612722	-0.4987	2017-12-21T02:05:40	1-2-3-4	0.79	noAO
NGC1087 P03	41.612686	-0.48263	2017-12-21T03:09:30	1-2-3	0.83	noAO
			2017-12-21T03:56:29	1-2		
NGC1087 P04	41.596478	-0.48255	2018-01-12T01:32:38	1-2-3-4	0.63	noAO
NGC1087 P05	41.596292	-0.51499	2018-01-10T01:43:24	1-2-3-4	0.84	noAO
NGC1087 P06	41.612674	-0.51478	2018-01-11T01:02:44	1-2-3-4	0.63	noAO
NGC1300 P01	49.921565	-19.41124	2019-02-03T01:41:13	1-2-3-4	0.78	AO
NGC1300 P02	49.904626	-19.41147	2019-08-29T09:19:34	1-2	0.66	AO
NGC1300 P03	49.938663	-19.41111	2019-09-25T07:57:43	1-2-3-4	0.75	AO
NGC1300 P04	49.93881	-19.42729	2019-10-08T07:39:28	1-2-3-4	0.81	AO
NGC1300 P05	49.904584	-19.39516	2019-12-02T04:41:28	1-2-3-4	0.54	AO
NGC1300 P06	49.921554	-19.39518	2019-12-03T05:12:50	1-2-3-4	0.50	AO
NGC1300 P07	49.938568	-19.39515	2019-12-21T00:55:54	1-2-3-4	0.63	AO
NGC1300 P08	49.955684	-19.40844	2019-12-23T01:39:45	1-2-3-4	0.56	AO
NGC1300 P09	49.921481	-19.42735	2019-12-22T01:34:49	1-2-3-4	0.58	AO
NGC1300 P10	49.904615	-19.4272	2019-12-22T02:42:19	1-2-3-4	0.62	AO
NGC1300 P11	49.887401	-19.42193	2020-01-16T01:26:09	1-2-3-4	0.54	AO
NGC1300 P12	49.887328	-19.4058	2020-01-16T02:41:23	1-2-3-4	0.69	AO
NGC1365 P01	53.421733	-36.14044	2018-01-10T02:49:23	1-2-3-4	0.71	noAO
NGC1365 P02	53.381807	-36.1409	2018-10-17T07:19:24	1-2-3-4	0.82	noAO
NGC1365 P03	53.401334	-36.12483	2018-01-20T01:16:28	1-2-3-4	0.83	noAO
NGC1365 P04	53.381516	-36.12465	2018-01-20T02:25:06	1-2-3-4	0.90	noAO
NGC1365 P05	53.421647	-36.12486	2018-10-16T05:26:10	1-2-3-4	0.92	noAO
NGC1365 P06	53.381737	-36.15673	2018-11-05T05:41:35	1-2-3-4	0.72	noAO
NGC1365 P07	53.401428	-36.15677	2018-11-06T05:32:56	1-2-3-4	0.64	noAO
NGC1365 P08	53.421804	-36.15702	2018-11-07T04:30:38	1-2-3-4	0.90	noAO
NGC1365 P09	53.441205	-36.14062	2018-12-04T03:58:31	1-2-3	0.90	noAO
NGC1365 P10	53.441226	-36.12449	2018-12-04T04:53:10	1-2-3-4	1.08	noAO
NGC1365 P11	53.361474	-36.14065	2018-12-05T04:08:13	1-2-3	0.58	noAO
NGC1365 P12	53.361534	-36.15674	2018-12-05T05:18:24	1-2-3-4	0.76	noAO
NGC1365 P30	53.402083	-36.14056	2014-10-12T04:31:28	1-2-3-4	0.82	noAO
			2014-10-12T05:30:02	1-2-3-4		
NGC1385 P01	54.378854	-24.50028	2019-10-06T08:06:01	1-2-3-4	0.49	AO
NGC1385 P02	54.360994	-24.50053	2019-12-31T03:56:25	1-2	0.38	AO

Galaxy & Pointing ID	RA °	DEC °	TPL start	Exposure #	PSF (FWHM) ″	MUSE mode WFM
			2019-12-31T04:55:57	1-2		
NGC1385 P03	54.369803	-24.48441	2020-01-20T01:12:41	1-2-3-4	0.57	AO
			2020-01-20T02:12:43	1-2-3-4		
NGC1385 P04	54.369803	-24.48441	2020-12-05T02:17:13	1-2-3-4	0.69	AO
NGC1385 P05	54.378854	-24.51639	2020-01-21T01:14:06	1-2-3-4	0.59	AO
NGC1433 P01	55.506902	-47.22178	2018-10-16T06:52:54	1-2-3-4	0.70	AO
NGC1433 P02	55.530064	-47.22185	2019-10-05T06:48:42	1-2-3-4	0.63	AO
NGC1433 P03	55.553469	-47.2217	2019-10-05T07:57:53	1-2-3-4	0.83	AO
NGC1433 P04	55.483191	-47.22189	2019-10-06T06:02:47	1-2-3-4	0.60	AO
NGC1433 P05	55.459083	-47.22203	2019-10-07T06:46:16	1-2-3	0.63	AO
			2019-10-07T07:59:06	1		
NGC1433 P06	55.45893	-47.2055	2019-11-02T04:33:56	1-2-3-4	0.65	AO
NGC1433 P07	55.482862	-47.20541	2019-11-20T02:08:18	1-2-3	0.70	AO
			2019-11-20T03:09:00	1		
NGC1433 P08	55.506986	-47.20549	2019-11-21T02:11:14	1-2-3-4	0.65	AO
NGC1433 P09	55.530772	-47.20538	2019-11-22T06:27:26	1-2-3-4	0.71	AO
NGC1433 P10	55.554174	-47.20554	2019-12-20T04:30:19	1-2-3-4	0.62	AO
NGC1433 P11	55.553626	-47.23813	2019-12-21T02:16:23	1-2-3-4	0.61	AO
NGC1433 P12	55.529952	-47.23809	2019-12-21T04:27:47	1-2-3-4	0.65	AO
NGC1433 P13	55.506442	-47.23789	2019-12-22T04:24:22	1-2	0.65	AO
			2019-12-22T05:05:18	1-2		
NGC1433 P14	55.482729	-47.23792	2019-12-23T03:48:53	1-2-3-4	0.51	AO
NGC1433 P15	55.459171	-47.23791	2019-12-30T03:38:48	1-2-3-4	0.64	AO
NGC1512 P01	60.998425	-43.34935	2018-12-30T01:11:52	1-2-3-4	0.73	noAO
NGC1512 P02	60.997871	-43.33288	2018-12-30T03:46:33	1-2-3-4	0.85	noAO
NGC1512 P03	60.976057	-43.3331	2018-02-17T01:02:45	1-2-3-4-5	1.18	noAO
NGC1512 P04	60.953684	-43.33286	2018-02-18T01:08:42	1-2-3-4	0.80	noAO
NGC1512 P05	60.953722	-43.34897	2018-02-19T01:04:07	1-2-3-4	0.68	noAO
NGC1512 P06	60.954141	-43.36546	2019-01-10T02:41:43	1-2-3-4	0.70	noAO
NGC1512 P07	60.976389	-43.36524	2019-01-10T03:47:10	1-2-3-4	0.83	noAO
NGC1512 P08	60.998479	-43.36538	2019-01-10T04:52:57	1-2-3-4	0.93	noAO
NGC1512 P30	60.975987	-43.34905	2017-09-21T06:53:05	1	0.64	noAO
			2017-09-21T08:30:27	1-2		
			2017-09-22T08:39:40	1		
NGC1566 P01	65.030061	-54.93785	2018-12-14T03:12:39	1-2-3-4	0.54	AO
NGC1566 P02	64.974665	-54.93714	2019-01-15T02:28:00	1-2-3-4	0.56	AO
NGC1566 P03	65.013148	-54.95397	2020-12-10T04:30:27	1-2-3-4	0.60	AO
NGC1566 P04	64.985261	-54.92184	2019-01-25T00:53:23	1-2-3-4	0.65	AO
NGC1566 P05	65.013286	-54.92178	2019-01-27T00:52:13	1-2-3-4	0.63	AO
NGC1566 P06	64.985399	-54.95382	2019-01-27T02:02:45	1-2-3-4	0.72	AO
NGC1566 P07	65.011776	-54.9057	2019-01-28T01:09:07	1-2-3-4	0.64	AO
NGC1566 P30	65.001794	-54.93786	2017-10-23T04:45:57	1-2-3-4	0.64	AO
NGC1672 P01	71.444433	-59.25258	2017-11-12T06:54:01	1-2-3-4	0.65	noAO
NGC1672 P02	71.440988	-59.23654	2017-12-23T04:11:46	1-2-3-4	0.89	noAO
NGC1672 P03	71.410094	-59.23802	2017-11-13T06:07:01	1-2-3-4	0.73	noAO
NGC1672 P04	71.412987	-59.25384	2017-11-25T05:07:09	1-2-3-4	0.65	noAO
NGC1672 P05	71.475798	-59.25114	2017-12-26T05:11:09	1-2-3-4	0.80	noAO
NGC1672 P06	71.47238	-59.23514	2017-12-19T04:31:59	1-2-3-4	0.77	noAO
NGC1672 P07	71.377135	-59.23943	2017-12-19T05:38:10	1-2-3-4	0.71	noAO
NGC1672 P08	71.381706	-59.25546	2018-01-11T02:26:31	1-2-3-4	0.68	noAO
NGC2835 P01	139.47034	-22.33869	2017-12-15T06:22:14	1-2-3-4	0.78	noAO
NGC2835 P02	139.470252	-22.37082	2018-01-16T07:38:48	1-2-3-4	1.08	noAO
NGC2835 P03	139.487844	-22.36179	2018-01-18T03:42:20	1-2-3-4	0.93	noAO
NGC2835 P04	139.487928	-22.3458	2018-01-23T03:26:36	1-2-3-4	0.67	noAO
NGC2835 P05	139.452986	-22.34596	2018-02-14T02:03:35	1-2-3-4	0.85	noAO
NGC2835 P06	139.452841	-22.36209	2018-02-20T01:20:57	1-2-3-4	0.71	noAO
NGC2835 P30	139.470371	-22.35446	2017-02-02T02:58:32	1-2-3-4	0.87	noAO
NGC3351 P01	161.007339	11.7042	2019-02-10T04:59:15	1-2-3-4	0.71	noAO
NGC3351 P02	160.974424	11.7042	2019-02-10T06:03:50	1-2-3-4	0.76	noAO
NGC3351 P03	160.990893	11.68806	2019-03-02T03:17:26	1-2-3-4	0.66	noAO

Galaxy & Pointing ID	RA °	DEC °	TPL start	Exposure #	PSF (FWHM) ″	MUSE mode WFM
NGC3351 P04	160.990873	11.72028	2019-03-02T04:16:25	1-2-3-4	0.73	noAO
NGC3351 P05	161.007392	11.68802	2019-03-03T03:51:18	1-2-3-4	0.82	noAO
NGC3351 P06	160.974484	11.72025	2019-03-03T05:02:01	1-2-3-4	0.98	noAO
NGC3351 P07	161.007289	11.72022	2019-03-11T02:49:48	1-2-3-4	0.84	noAO
NGC3351 P08	160.974375	11.68819	2019-03-12T02:42:02	1-2-3-4	0.74	noAO
NGC3351 P30	160.990417	11.70381	2016-03-30T00:04:22	1-2-3-4	0.61	noAO
			2016-04-04T00:43:01	1-2-3-4		
NGC3627 P01	170.072929	12.98949	2018-01-25T07:19:09	1-2-3-4	0.68	noAO
NGC3627 P02	170.055847	12.98976	2018-05-13T23:25:01	1-2-3-4	0.78	noAO
NGC3627 P03	170.054709	12.97342	2018-05-08T01:35:58	1-2-3-4	0.98	noAO
NGC3627 P04	170.071261	12.97362	2018-05-14T00:35:00	1-2-3-4	0.75	noAO
NGC3627 P05	170.072366	13.0058	2018-05-14T01:41:04	1-2-3-4	0.80	noAO
NGC3627 P06	170.056162	13.00601	2018-05-14T23:25:02	1-2-3-4	0.77	noAO
NGC3627 P07	170.054957	12.95769	2018-05-15T00:29:52	1-2-3-4	0.74	noAO
NGC3627 P08	170.071501	12.95767	2018-05-15T01:34:18	1-2-3-4	0.81	noAO
NGC4254 P01	184.713694	14.41518	2018-04-16T02:49:03	1-2-3-4-5	0.63	AO
NGC4254 P02	184.697794	14.4153	2018-05-19T02:22:33	1-2-3-4	0.57	AO
NGC4254 P03	184.714741	14.43107	2018-06-08T00:17:56	1-2-3-4	0.59	AO
NGC4254 P04	184.697599	14.43081	2018-06-08T23:17:55	1-2-3-4	0.61	AO
NGC4254 P05	184.708005	14.39908	2018-06-04T23:35:32	1-2	0.81	AO
			2018-06-05T00:11:22	1-2-3		
NGC4254 P06	184.691941	14.39909	2018-06-05T01:06:43	1-3-4	0.77	AO
NGC4254 P07	184.724544	14.39901	2018-06-09T23:26:07	1-2-3-4	0.62	AO
NGC4254 P08	184.730498	14.41463	2018-06-06T23:44:42	1-2-3-4	0.48	AO
NGC4254 P09	184.731384	14.43116	2018-06-13T00:04:09	1-2-3	0.45	AO
			2018-06-13T00:51:40	1		
NGC4254 P10	184.698343	14.44673	2019-03-11T04:59:39	1-2-3-4	0.53	AO
NGC4254 P11	184.714996	14.44694	2019-03-02T05:27:50	1-2-3-4	0.44	AO
NGC4254 P12	184.731621	14.44696	2019-03-02T06:35:48	1-2-3-4	0.45	AO
NGC4303 P01	185.478821	4.47383	2019-05-10T03:10:00	1	0.55	AO
			2019-05-10T03:51:19	1-2-3		
NGC4303 P02	185.494958	4.47371	2019-05-27T23:39:52	1-2-3-4	0.64	AO
NGC4303 P03	185.462592	4.47361	2019-06-29T23:25:58	1-2-3	0.59	AO
			2019-06-30T00:26:58	1		
NGC4303 P04	185.478627	4.48972	2020-01-30T07:08:21	1-2	0.54	AO
			2020-01-30T07:43:58	1-2		
NGC4303 P05	185.47875	4.4575	2020-02-03T06:23:31	1-2-3-4	0.58	AO
NGC4303 P06	185.494912	4.48972	2020-02-03T07:35:27	1-2-3-4	0.53	AO
NGC4303 P07	185.494788	4.45766	2020-02-28T07:39:20	1	0.51	AO
			2020-02-28T08:05:55	1-2-3		
NGC4303 P08	185.462442	4.48974	2020-02-19T05:54:25	1-2-3-4	0.61	AO
NGC4303 P09	185.462532	4.45765	2020-02-19T07:35:28	1-2-3-4	0.70	AO
NGC4321 P01	185.734704	15.8219	2019-04-28T02:38:38	1-2-3-4	0.79	AO
NGC4321 P02	185.717999	15.82332	2019-04-30T02:20:03	1-2-3-4	0.59	AO
NGC4321 P03	185.750833	15.82194	2019-05-01T01:06:01	1-2-3-4	0.85	AO
NGC4321 P04	185.73408	15.83803	2020-03-02T06:11:38	1-2-3-4	0.47	AO
NGC4321 P05	185.717559	15.83938	2020-03-03T06:06:28	1-2-3-4	0.72	AO
NGC4321 P06	185.734316	15.80579	2020-02-20T07:07:56	1-2-3	0.46	AO
			2020-02-20T08:03:06	1		
NGC4321 P07	185.717498	15.80723	2020-03-18T05:09:33	1-2-3-4	0.61	AO
NGC4321 P08	185.751212	15.80621	2021-02-12T06:35:52	1-2-3-4	1.00	AO
NGC4321 P09	185.700805	15.82756	2020-03-22T04:56:36	1-2-3-4	0.50	AO
NGC4321 P10	185.701823	15.84284	2020-03-23T04:43:09	1-2-3-4	0.67	AO
NGC4321 P11	185.750833	15.83806	2020-03-24T04:28:48	1-2-3-4	1.09	AO
NGC4535 P01	188.576744	8.19195	2018-04-09T03:18:03	1-2-3-4	0.47	AO
NGC4535 P02	188.593278	8.19259	2018-04-09T04:46:39	1-2-3-4	0.43	AO
NGC4535 P03	188.592956	8.20803	2018-04-10T02:42:01	1-2-3-4	0.43	AO
NGC4535 P04	188.576548	8.20801	2018-04-14T04:31:10	1-2-3-4	0.47	AO
NGC4535 P05	188.592752	8.17594	2018-04-16T04:53:52	1-2-3-4	0.44	AO
NGC4535 P06	188.576717	8.1758	2018-05-17T00:00:23	1-2-3-4	0.43	AO

Galaxy & Pointing ID	RA °	DEC °	TPL start	Exposure #	PSF (FWHM) ″	MUSE mode WFM
NGC5068 P01	199.729433	-21.04312	2018-05-14T02:48:05	1-2-3-4	0.67	noAO
			2018-06-14T02:46:50	1-2-3		
NGC5068 P02	199.729986	-21.02694	2018-05-14T04:20:06	1-3-4	0.88	noAO
NGC5068 P03	199.711794	-21.04348	2018-05-15T02:42:20	1-2-3-4	0.96	noAO
NGC5068 P04	199.712242	-21.02699	2018-05-20T02:58:19	1-2-3-4	0.69	noAO
NGC5068 P05	199.745845	-21.04327	2018-05-21T04:13:30	1-2-3-4	0.62	noAO
NGC5068 P06	199.72313	-21.05915	2018-06-15T02:09:06	1-2-3-4	0.83	noAO
NGC5068 P07	199.705524	-21.0592	2018-06-17T01:57:12	1-2-3-4	0.77	noAO
NGC5068 P08	199.712023	-21.01147	2018-07-10T23:50:45	1-2-3-4	0.56	noAO
NGC5068 P09	199.695073	-21.01376	2018-07-11T00:56:19	1-2-3-4	0.52	noAO
NGC5068 P10	199.740055	-21.05934	2018-07-14T00:44:22	1-2-3-4	0.90	noAO
NGC7496 P01	347.4467	-43.42833	2019-06-09T08:31:41	1	0.62	AO
			2019-06-09T08:53:47	1-2-3		
NGC7496 P02	347.440551	-43.41284	2019-07-04T08:15:45	1-2	0.81	AO
			2019-07-04T09:23:58	1-2-3		
NGC7496 P03	347.452917	-43.44361	2019-08-25T06:43:38	1-2-3-4	0.79	AO

This PHANGS-MUSE data release includes both data cubes and derived products.

For each galaxy we release:

- Mosaiced data cubes at *native* resolution (including variance and quality cubes).
- Mosaiced data cubes at convolved and optimised (*copt*) resolution (including variance cubes). The PSF of these mosaics has been homogenised spatially across the galaxy and as a function of wavelength.
- Mosaiced data products at *native* resolution.
- Mosaiced data products at convolved and optimised (*copt*) resolution, derived from the copt data cubes as described above

The derived data products are as follows (Tables 3 and 4):

Derived parameter	Description
	Stellar kinematics
`BIN_ID`	unique ID for each Voronoi bin
`V_STARS`	stellar velocity [km s^{-1}], after subtracting the systemic velocity
`FORM_ERR_V_STARS`	formal velocity error [km s^{-1}]
`SIGMA_STARS`	stellar velocity dispersion [km s^{-1}]
`FORM_ERR_SIGMA_STARS`	formal sigma error [km s^{-1}]
	Emission lines `*emline` = emission line string id listed in the following table
`*emline_FLUX`	emission line flux [10^{-20} erg s^{-1} cm^{-2} $spaxel^{-1}$]
`*emline_FLUX_ERR`	emission line flux error [10^{-20} $ergs^{-1}cm^{-2}$ $spaxel^{-1}$]
`*emline_VEL`	emission line velocity [km s^{-1}]
`*emline_VEL_ERR`	emission line velocity error [km s^{-1}]
`*emline_SIGMA`	emission line velocity dispersion [km s^{-1}]
`*emline_SIGMA_ERR`	emission line velocity dispersion error [km s^{-1}]

Table 3: *list of data products and their corresponding names.*

Emission line velocity dispersions (*emline_SIGMA) are not deconvolved from the instrumental resolution. The instrumental dispersion as a function of wavelength has been previously derived in Bacon et al. (2017). In this data release, emission line properties are made available for the following lines:

line name	Wavelength (air) [Å]	String ID	Ionisation potential [eV]	Fixed ratio
		Hydrogen Balmer lines		
Hβ	4861.35	HB4861	13.60	no
Hα	6562.79	HA6562	13.60	no
		Low ionisation lines		
[N II]λ6548	6548.05	NII6548	14.53	0.34 [N II]λ6584
[N II]λ6584	6583.45	NII6583	14.53	no
[S II]λ6717	6716.44	SII6716	10.36	no
[S II]λ6731	6730.82	SII6730	10.36	no
		High ionization lines		
[O III]λ4959	4958.91	OIII4958	35.12	0.35 [O III]λ5007
[O III]λ5007	5006.84	OIII5006	35.12	no

Table 4: *list of emission lines covered by this PHANGS-MUSE data release*

Release Notes

We aimed at an almost fully automated pipeline that could be easily tuned to specific needs and potential changes associated with the survey and science goals. Please see https://pypi.org/project/pymusepipe/ and Emsellem et al. (2021) for a detailed description of all data reduction steps.

The MUSE data reduction pipeline (Weilbacher et al. 2020; v2.8.1) is used to remove the instrumental signatures. This includes bias and flat field corrections, wavelength and line spread function (lsf) calibration based on the facility arc lamp calibrations, as well as geometric and astrometric alignment. Wavelength solutions are provided in the barycentric reference system. Absolute solutions for the astrometric and photometric calibrations are derived from R-band imaging acquired in the course of the PHANGS project (PHANGS-Halpha, A. Razza et al. in preparation), and are tied to absolute calibration from Gaia (DR1) sources in those broadband fields. Satellite trails are masked as needed within individual science exposures. All wavelengths refer to air wavelengths.

Data Reduction and Calibration

Data Cubes - Photometric calibration and sky subtraction

Offset sky exposures are used to produce a sky spectrum. We then used the reference R-band images to simultaneously constrain the sky subtraction and the global flux normalisation (per exposure). Assuming that the R-band reference image has zero background and the correct absolute flux normalisation, and that the flux in the MUSE reconstructed image represents a linear function of the true flux (involving a normalisation constant plus a background), we can write:

$$\begin{aligned} \mathrm{Flux}_{\mathrm{Rband}}(x,y) &= a \times \mathrm{MUSE}_1^R(x,y) \\ &= a \times \left(\mathrm{MUSE}_{\mathrm{raw}}^R(x,y) + \mathrm{Sky} - \mathrm{Sky}_1\right) + b \end{aligned}$$

where Sky is a constant representing the true sky background for that specific exposure, Sky_1 is another constant representing the actual value removed during the initial sky subtraction process, and a and b are constants representing a linear regression representation of the $\mathrm{Flux}_{\mathrm{Rband}}$ versus the MUSE reconstructed image. A perfect sky subtraction and normalisation would lead to a=1 and b=0. We then use the fitted a value as a normalisation correction, and b to fix the sky contribution by applying $Sky = \alpha \times Sky_1$ where $\alpha = 1 - b/(a \cdot Sky_1)$. Hence, knowing a and b as well as Sky_1, the value of the sky continuum

integrated within the reference image filter, we derive a correction for the sky normalisation that yields a linear regression where b=0.

It is important to note that the sky renormalisation only acts within the R-band filter, assuming that the reference image is background free. Since the reference MUSE sky exposure may result in a reference sky spectrum that is not necessarily an exact representation of the actual sky on the MUSE science exposure, this could lead to a colour variation, hence to an over- or under-subtraction of the sky which depends on wavelength.

Data Cubes - Image reconstruction

We follow an approach that minimises the need for resampling steps, using a table-based (PixTable) representation of the data, as implemented in the MUSE data reduction scripts. The PixTables and cubes are themselves used to reconstruct images in specific filters or extract spectra. For individual pointings, this is straightforward. For our mosaiced data products, which combine all observations across the galaxies, we take two approaches:

Native resolution - "native"

Mosaiced datacubes whose astrometry and background levels have been calibrated to match those of the reference R-band images were computed. We refer to these mosaics as "native" (for native spatial resolution): the variation of the PSF over the field and as a function of wavelength is not corrected. The native datacubes have the advantage of having the highest spatial resolution possible with the given observations, while the PSF variation may impair robust measurements throughout the FoV, or depending on wavelength. The range of PSF values across these native resolution mosaics is given above in the sample table.

Convolved and optimized resolution - "copt"

Given the combination of multiple individual science observations, allowing for rotations at each position and multiple positions across each galaxy, our combined mosaics have Point-Spread-Functions (PSFs) that are varying over the spatial FoV and spectral range (see Sec. 4.2.6 in Emsellem et al 2021). *pypher*[1] (Boucaud et al. 2016) provides a robust tool to derive kernel cubes feeding a Fast Fourier Transform-based convolution algorithm to homogenise the end-product MUSE datacubes. Given two arbitrary PSF images, the *pypher* software uses a Wiener filter with a regularisation parameter to compute the convolution kernel needed to move from the input PSF to the output one. The power of such an algorithm is its applicability to general PSFs, expressed analytically or not. We used *pypher* to move from the wavelength-dependent circular Moffat PSF typical of the MUSE spectrograph, to a wavelength-independent circular Gaussian.

Our target PSF is a circular two-dimensional Gaussian whose FWHM is constant as a function of wavelength and position within each individual mosaic. A Gaussian target PSF was selected to simplify further post-processing, including, e.g., convolution to coarser spatial resolutions. The final copt PSF for each galaxy is listed above in the sample table.

Data Products - Stellar continuum fitting

Prior to the fitting process, the MUSE data cube is corrected for foreground Galactic extinction, using the O'Donnell et al. (1994) extinction law and the $E(B-V)$ values from Schlafly et al. (2011; see sample table above). The data are then Voronoi binned to a target S/N of 35. This S/N level is used to determine both the stellar kinematics and the stellar population properties. The stellar kinematics are derived using *pPXF*[2] (Cappellari & Emsellem 2004, Cappellari 2017), following the same procedure as implemented

[1] https://pypi.org/project/pypher/
[2] https://pypi.org/project/ppxf/

by Bittner et al. (2019) in *gist*[3]. Note that the data cubes provided in the data release are "as observed" and thus do not include any correction for extinction (which is only applied during the analysis process).

Briefly, to fit the stellar continuum we use E-MILES simple stellar population models (Vazdekis et al. 2016), generated with a Chabrier et al. (2003) initial mass function, BaSTI isochrones (Pietrinferni et al. 2004), eight ages (0.15 -14 Gyr, logarithmically spaced in steps of 0.22 dex) and four metallicities ([Z/H] = [-1.5, -0.35, 0.06, 0.4]), for a total of 32 templates. We fit the wavelength range 4850 - 7000 Å in order to avoid strong sky residuals in the redder part of the MUSE wavelength range. The regions around the expected positions of ionised gas emission lines and sky lines are masked. To derive the stellar kinematics we make use of additive Legendre polynomials (12th order, in the spectral direction), and no multiplicative polynomials.

Data Products - Emission line fitting

The MUSE data cube is corrected for foreground Galactic extinction as for the stellar continuum fitting process. The fits are performed on individual spaxels, and the stellar kinematics is fixed to that of the Voronoi bin to which the spaxel was associated during the stellar kinematics fitting step.

Emission lines are fitted by performing an independent call to *pPXF*, where emission lines are treated as additional Gaussian templates, and the stellar continuum is fitted simultaneously. Some of the code we use to interface with *pPXF* in this fitting stage was adapted directly from the MaNGA data analysis pipeline (Westfall et al. 2019), and makes use of the analytical Fourier transform implemented in version > 6 of *pPXF* (Cappellari et al. 2017).

The kinematic parameters of the emission lines (velocity and velocity dispersion) are tied in three groups, as follows:

1. Hydrogen Balmer lines: Hα, Hβ;
2. Low-ionisation lines: [O I]$\lambda\lambda$6300,64, [N I]$\lambda\lambda$5197,5200, [N II]$\lambda\lambda$6548,84, [N II]λ5754, [S II]$\lambda\lambda$6717,31;
3. High-ionisation lines: [He I]λ5875, [O III]$\lambda\lambda$4959,5007, [S III]λ6312.

Only emission lines from Hα, Hβ, [OIII], [NII] and [SII] are included in this release.

We tie the intrinsic (astrophysical) velocity dispersion within each kinematic group, prior to convolution with the instrumental LSF. During the emission lines fit, *pPXF* is run with 8th order multiplicative Legendre polynomials, but no additive polynomials.

[3] https://abittner.gitlab.io/thegistpipeline/V3.0.4-doc1/

Data Quality

Here we report a short summary of the data quality (see e.g., Figures 2, 3 and 4). More details can be found in Emsellem et al. (2021), where the following figures have been taken from.

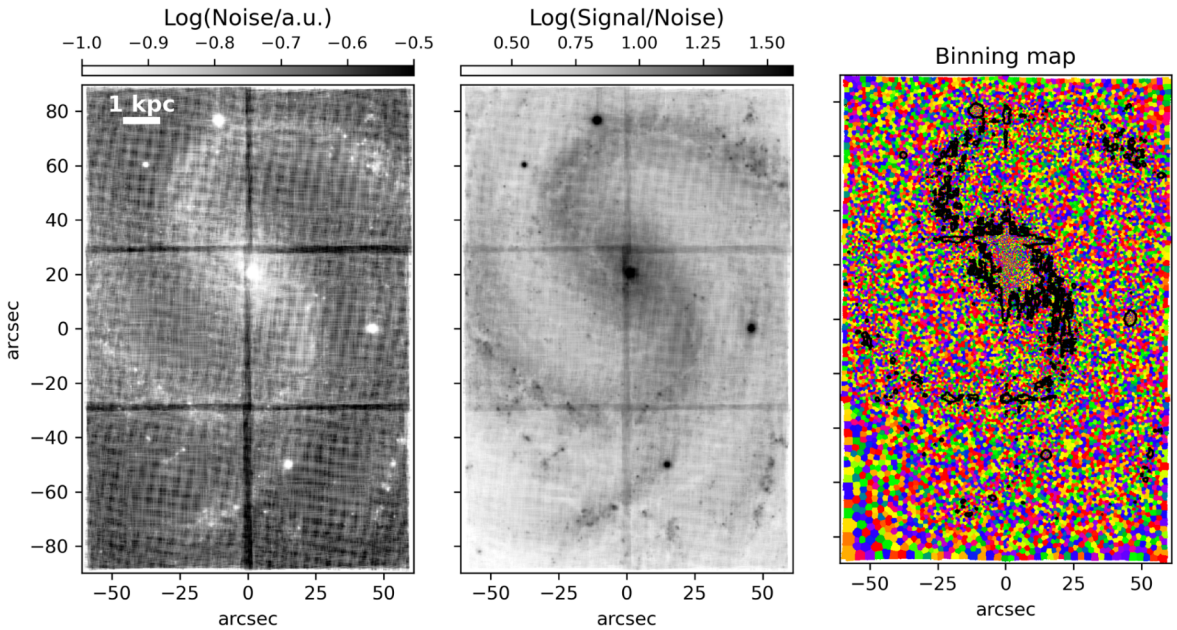

Figure 2: Noise and signal-to-noise ratio

Maps of the average noise (left panel), Signal/Noise (S/N; middle panel) and binning map (right panel) for NGC4535. The noise and S/N maps are computed by averaging the pipeline noise and flux over the 5300-5500 Å wavelength range. The stripes dividing the surveyed area into six squared subregions correspond to the overlap regions of the six MUSE pointings obtained for this galaxy. The noise map also shows an evident cross-hatch pattern within individual pointings, due to the cube-generating resampling step in the MUSE data reduction pipeline when combining exposures with different rotation angles. This behaviour is also visible in the S/N map, but does not significantly affect the results of the binning process. The binning map shows the result of the Voronoi binning procedure with target S/N=35. The black contour shows the S/N = 12 level on individual spaxels. In this target only the galaxy centre (and a few foreground stars) have S/N > 35 in individual spaxels, which are therefore left unbinned.

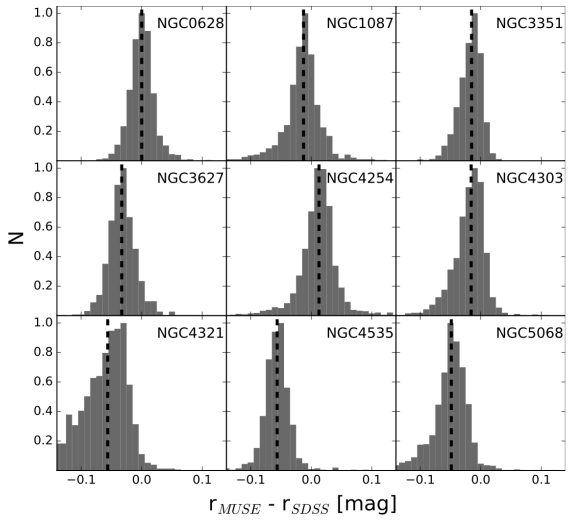

Figure 3: Absolute photometry

To validate the overall absolute photometric calibration of the cubes, we compare synthetic broad-band images against existing SDSS images for the nine galaxies that lie within the SDSS legacy survey footprint. Here we compare r-band magnitudes measured over 5" x 5" apertures within MUSE synthetic images (r_{MUSE}) and SDSS images (r_{SDSS}) for the nine galaxies with SDSS imaging available. Histograms are normalized for each galaxy and the median offset is indicated with a dashed line. Across this sample of galaxies, the median offset ranges from -0.06 to 0.01 mag. The typical scatter within any galaxy is ~0.04 mag. This is roughly consistent with the SDSS photometric calibration uncertainty (Padmanabhan et al. 2008).

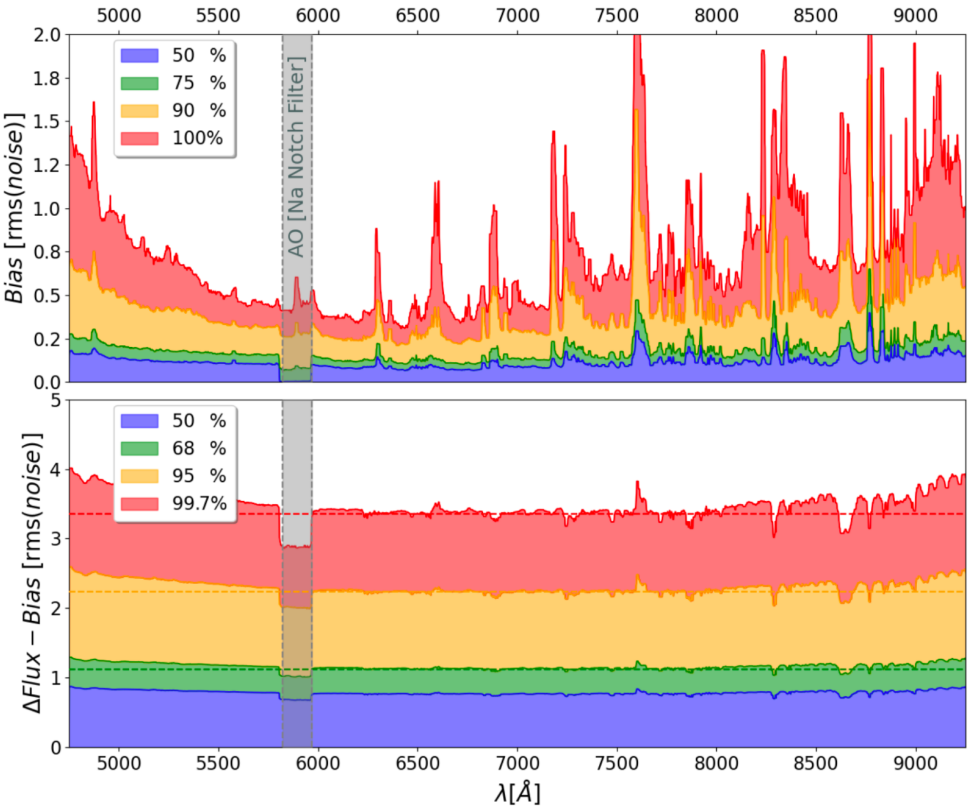

Figure 4: Spectrophotometry

Median offset and percentiles of the difference between spectra of the same regions from overlapping pointings. The statistics have been computed from a set of about 250 regions covering the full

PHANGS-MUSE sample, and the resulting percentile vectors have been filtered to make it legible (keeping the sky line residuals visible). Top panel: percentiles of the distribution of the bias level, normalised by the typical (overlap-region-averaged) noise level. 90% of the spectra have a bias which is typically between 30 and 50% of the noise level, while a small fraction shows up at levels of 60-120% of the noise, specifically in the blue or red part of the spectrum. Note that although beyond 7000 Å residuals are heavily contaminated by sky line residuals, the pipeline still constructs a roughly correct noise vector. Bottom panel: percentiles (50, 68.3, 95.5%, and 99.7%) of the distribution of differences normalised by the individual spectra noise level, after subtraction of a wavelength-independent median `bias' offset (see Emsellem et al. 2021 for more details). The dashed (respectively, green, yellow, and red) lines show values of 1.12 (12% above 1), 2.24, and 3.36, showing that the noise level is slightly under-estimated (by about 12%). A trend is visible towards the redder and bluer end of the wavelength coverage.

Absolute astrometry

To validate the astrometric solution of the MUSE data, we compared the positions of stars in the MUSE mosaics (as defined in Sec. 5.2 of Emsellem et al. 2021) with their locations in our broadband R-band imaging. When comparing the MUSE positions with the broadband positions (measured with the same procedure), we obtain ΔRA = 0.026”± 0.047” and ΔDec = -0.013” ± 0.044”: such values are observed consistently across the full PHANGS-MUSE sample and are well within the accuracy expected from our alignment routine, representing only from about ⅕th to 1/20th of a MUSE spaxel size.

Known issues

Image alignment

We identified a few issues associated with the geometric and astrometric solutions provided via predefined MUSE calibrations. About 20% of all exposures exhibit a global small but still significant rotation between 0.1 and 0.3 degrees with respect to the R-band images, with no apparent correlation with RA, DEC or time when the target was observed. This residual rotation is corrected for.

Imperfect sky subtraction: effect on stellar extinction

Overall, we conclude that we may slightly under-estimate the noise level by 10 to 30% when using the derived variances (and ignoring the covariance terms), and that the `bias' due to improper sky continuum subtraction is present and negligible for most of the spectra, but can be significant for about 10 to 20% of them, especially towards the blue end of the MUSE wavelength range.

By construction, there are no offsets in the broad-band color reconstructed images of individual pointings. We confirm that we observe no systematic differences between adjacent pointings using such broad-band filters, a good a posteriori check of our implementation. This is, however, not necessarily true for colors. The spectral dependence of the median bias suggests that the shape of the sky continuum spectrum used for the sky background subtraction process may sometimes depart from the true one. Fixing such an issue would require a spectrally-dependent correction of the reference sky spectrum itself. This may be addressed by using photometric reference points (e.g., HST imaging) in several bands (as opposed to the single R_c band used here), but it is beyond the scope of the present release.

Previous Releases

N/A

Data Format

Files Types

Detailed information on the data reduction and analysis process have been reported in the "Release Notes" section of this document and in Emsellem et al. 2021. In this section, we focus on the naming convention of the files. When present, the string {gal_name} should be replaced with the name of the galaxies in capital letters (e.g., "NGC4303") and the string {psf} should be replaced with the homogenised PSF FWHM (2 digits, e.g. "0.78"). The galaxy names and the FWHM of the homogenised PSF can be found in Table 1 of this document.

The main released data products are the mosaiced datacubes of the galaxies. The datacubes for the single pointings are not included in this data release. The files are named using the following naming convention:

- `{gal_name}_PHANGS_DATACUBE_native.fits (PRODCATG=SCIENCE.CUBE.IFS)`
  Reduced mosaic of the galaxy in native resolution (i.e. the PSF has not been homogenised). It is a multi-extension fits file with three extensions: the data extension (EXTNAME=DATA), the variance extension (EXTNAME=STAT) and the data quality extension (EXTNAME=DQ).

- `{gal_name}_PHANGS_DATACUBE_copt_{psf}asec.fits (PRODCATG=SCIENCE.CUBE.IFS)`
  Reduced mosaic of the galaxy convolved to the worst (gaussian) PSF as described in the "Data Cubes - Image reconstruction" section of this document. The FWHM of the homogenised PSF can be recovered from the file name (e.g., 0.78asec) or from Table 1 of this document. The file contains the data, variance and data quality extensions as described for the native datacube.

Those datacubes are accompanied by several other ancillary data:

- `{gal_name}_PHANGS_IMAGE_{filter}_native.fits / {gal_name}_PHANGS_IMAGE_{filter}_copt_{psf}asec.fits (PRODCATG=ANCILLARY.IMAGE)`
  Broad-band images of the galaxies in native and copt resolution. These include a whitelight image (`{filter} = white`) and images in three SDSS broad-band filters (`{filter} = SDSS_r, SDSS_g, SDSS_i`). The fits files contain the three usual extensions: data (EXTNAME=DATA), variance (EXTNAME=STAT) and data quality (EXTNAME=DQ). Beware that the broad-band filters may actually not be entirely covered by the MUSE spectral coverage (the AO gap in the MUSE spectral coverage is linearly interpolated when present - when the AO mode is used).

- `{gal_name}_MAPS_native.fits / {gal_name}_MAPS_copt_{psf}asec.fits (PRODCATG=ANCILLARY.IMAGE)`
  This is a multi-extension fits file containing all the quantities measured when fitting the datacubes with *pPXF*. Two separate files are released, one for the *native* version of the datacubes, and one for the homogenised (*copt*) version. An exhaustive list of the included extensions and of their names can be found in Table 3 and 4 of the present document.

Catalogue Columns

No catalogs are released.

Acknowledgements

The PHANGS-MUSE survey, dataset and data reduction associated with this data release is described in detail in Emsellem et al. 2021 (submitted). Please cite the PHANGS-MUSE survey paper (Emsellem et al. 2021, submitted) when making use of this dataset. A link to the pdf file is provided here (its status will be updated in due time): phangs-muse_survey_paper_submitted.pdf.
The link is also available on the PHANGS web site: Publications

PHANGS-MUSE was only possible through the dedicated effort of several people over half a decade. The appendix of the PHANGS-MUSE survey paper outlines the contributions of the individual team members.

Please include the following/references acknowledgements when making use of this data:

Based on observations taken as part of the PHANGS-MUSE large program (Emsellem et al. 2021).
Based on data products created from observations collected at the European Organisation for Astronomical Research in the Southern Hemisphere under ESO programme(s) 1100.B-0651, 095.C-0473, and 094.C-0623 (PHANGS-MUSE; PI Schinnerer), as well as 094.B-0321 (MAGNUM; PI Marconi), 099.B-0242, 0100.B-0116, 098.B-0551 (MAD; PI Carollo) and 097.B-0640 (TIMER; PI Gadotti). This research has made use of the services of the ESO Science Archive Facility.

This research has made use of the services of the ESO Science Archive Facility.
Science data products from the ESO archive may be distributed by third parties, and disseminated via other services, according to the terms of the Creative Commons Attribution 4.0 International license.
Credit to the ESO origin of the data must be acknowledged, and the file headers preserved.

References

Anand, G. S., Lee, J.C., Van Dyk, S. D., et al. 2021, MNRAS, 501, 3621;

Bacon, R., Brinchmann, J., Richard, J., et al. 2015, A&A, 575, A75;

Bacon, R., Conseil, S., Mary, D., et al. 2017, A&A, 608, A1;

Bittner, A., Falcón-Barroso, J., Nedelchev, B., et al. 2019, A&A, 628, A117;

Bittner, A., Sánchez-Blázquez, P., Gadotti, D. A., et al. 2020, A&A, 643, A65;

Boucaud, A., Bocchio, M., Abergel, A., et al. 2016, A&A, 596, A63;

Calzetti, D. 2001, PASP, 113, 1449;

Cappellari, M. & Emsellem, E. 2004, PASP, 116, 138;

Cappellari, M. 2017, MNRAS, 466, 798 et al. 2017;

Carrillo, A., Jogee, S., Drory, N., et al. 2020, MNRAS, 493, 4094

Chabrier, G. 2003, PASP, 115, 763;

Emsellem, E., Schinnerer, E., Santoro, F., et al. 2021, A&A submitted[4]

Leroy, A. K., Sandstrom, K. M., Lang, D., et al. 2019, ApJS, 244, 24;

Leroy, A. K., Schinnerer, E., Hughes, A., et al. 2021, arXiv e-prints, arXiv:2104.07739;

[4] The submitted paper can be found here: Publications

O'Donnell J. E. 1994, ApJ, 422, 158;

Padmanabhan, N., Schlegel, D. J., Finkbeiner, D. P., et al. 2008, ApJ, 674, 1217;

Pietrinferni, A., Cassisi, S., Salaris, M., & Castelli, F. 2004, ApJ, 612, 168;

Schlafly, E. F. & Finkbeiner, D. P. 2011, ApJ, 737, 103;

Vazdekis, A., Koleva, M., Ricciardelli, E., Röck, B., & Falcón-Barroso, J. 2016,MNRAS, 463, 3409;

Weilbacher P. M., Palsa, R., Streicher, O., et al. 2020, A&A, 641, A28;

Westfall, K. B., Cappellari, M., Bershady, M. A., et al. 2019, AJ, 158, 231.